CrossMark

# In Situ Raman Observation of Zinc-Induced Structural Dynamics and Charge Transfer of a Layered V₂O₅

Chunjian Wang,[1,2] Weiping Xie,[1] Hongtao Cao,[1,2] Qiang Wang,[3] Chengli Zhang,[3] Guanglong Xu,[3] Junhua Gao,[1] and Hongliang Zhang[1,2,z]

$^1$*Laboratory of Advanced Nano Materials and Devices, Ningbo Institute of Materials Technology and Engineering, Chinese Academy of Sciences, Ningbo 315201, People's Republic of China*
$^2$*Center of Materials Science and Optoelectronics Engineering, University of Chinese Academy of Sciences, Beijing 100049, People's Republic of China*
$^3$*Ningbo Wakan Electronic Science Technology Co. LTD., Ningbo 315475, People's Republic of China*

In situ techniques to disclose electrochemical and interfacial behavior between electrode and electrolyte in a quantitative manner are in high demand in numerous fields including electrochromism, energy storage as well as basic science research. This work demonstrates a self-made in situ Raman spectra technique coordinating with an electrochemical workstation and its utility for zinc-induced structural dynamics and charge transfer of a layered $V_2O_5$. The increase or decrease of Raman activity modes of $V-O_3$, $O_1-V-O_2$ and $O_1-V-O_3$ at applied low or high voltages is probably due to the presence of "free pathway" within layers. An interpretation is proposed where the two stages of bidirectional reversibility of $Zn^{2+}$ intercalation and deintercalation from "free pathway" and $V_2O_5$ matrix occur via an electrochemical process, followed by $Zn^{2+}$ continuous aggregation, fusion and possible transformation to $Zn_xV_2O_5$. A distinct difference between $Li^+$-based and $Zn^{2+}$-based electrolytes is that the Raman active modes between V atom and apical oxygen are almost not enhanced or weakened for $V_2O_5$ in $Zn^{2+}$-based electrolyte, most likely due to the greater Coulomb force of $Zn^{2+}$ on $V_2O_5$ matrix than that of $Li^+$. These observations have implications for understanding the performance and stability of electrochromic devices.

Electrochromic materials, which dynamically change their colors in response to certain electrical stimuli, can be a powerful weapon to save energy when it is used for smart windows[1] which can modulate Sunlight in infrared wavelength. In addition to that, electrochromic material has potential applications in anti-glare mirrors,[2] military camouflage,[3] camera lens,[4] displays,[5] and so on. Since the debut of $WO_3$,[6] many other electrochromic materials, both organic and inorganic, have been under extensive research. Among the inorganic materials, $V_2O_5$ as a ploy-electrochromic material attracts a lot of recent research interest. $V_2O_5$, which can change its color from yellow to green, makes it a promising candidate for electrochromic displays, energy-saving camouflage, etc. In addition to that, due to the large interlayer distance and lower reduced valence of $V^{3+}$, $V_2O_5$ can achieve high capacity and high energy density when it is used as a battery cathode.[7] Combining the electrochromic property and energy storage ability of $V_2O_5$, an electrochromic battery can be constructed, which can module color while storing charge and in turn monitor battery status by colors.[8] All these practical applications depend on the reservable electrochemical reaction, structure transformation, and property of charge/discharge on the interface of the $V_2O_5$ electrode and electrolyte. A lot of effort has been made to improve the performance of $V_2O_5$. A nanostructured $V_2O_5$ with wide struts and a high surface-to-bulk volume ratio is reported, by which structure the $Li^+$ diffusion coefficient and electrical conductivity were improved.[9] Xiu-li Wang et al. reported a $SnO_2/V_2O_5$ core/shell structure, which can achieve multicolor change among yellow, green, and blue and explored its application for military camouflage.[3] Mo-doped $V_2O_5$ had a porous structure of the film and an increased ionic coefficient, and when it was coupled with $WO_3$ could make up to 10,000 cycles.[10] A carbon-coated $V_2O_5$ through annealing was constructed, which exhibited excellent electrochromic performance with a high optical modulation of 45.8%, a fast response time of 3.4 s, a high coloration efficiency of 89.3 $cm^2 C^{-1}$ and high cycling stability.[11]

In addition to the material itself, the inserted cations are another critical aspect that largely affects the performance of electrochemical

devices. Although $Li^+$ ion has advantages like long cycle life, high voltage, and high storage capacity, it has obvious drawbacks such as high cost, limited sources, and flammable electrolyte.[12] Therefore, many alternative cations have been under extensive research. Comparing with the monovalence cations, multivalence ions, like $Mg^{2+}$ and $Zn^{2+}$, have inert advantages since multiple charges can be provided during redox reaction and lower cost compared to lithium.[13] Among them, zinc excels other multivalence cations in many aspects, including low cost, non-toxic nature, multivalence, and small radius (0.074 nm), has been considered as a promising candidate in various electrochemical applications and has drawn a lot of attention.[14,15] Haizeng Li et al. reported improved capacity and electrochromic performance of Ti-substituted tungsten molybdenum oxide using $Zn^{2+}$ electrolyte, which exhibited high optical contrast of 76% and high areal capacity of 260 mAh m$^{-2}$.[16]

The performance of certain electrochemical devices significantly depends on interaction of conduction ions and active electrodes.[17] This interaction causes the constant changing of the interface of electrode and electrolyte thus studying of the interface is necessary. Among all the techniques, Raman spectroscopy is extremely sensitive to the local structure changes, which makes it a powerful tool to study the local structure variation of the sample.[18] A lot of work has been done to see the structure change of $V_2O_5$. Operando Raman spectroscopy was used by Angelique Jarry et al. to monitor the changes in $Li_xV_2O_5$ electronic structure and they found out the degradation was related to the drastic band structure changes with the deep discharge of $Li_xV_2O_5$.[19] To take a step forward, in situ Raman spectroscopy coordinated with electrochemistry, can form a powerful combination to probe the structure transformation under various environments.[20] Through in situ Raman spectroscopy, the in-time structure change of the targeted material can be gained, and therefore a deeper understanding of the mechanism of the interface can be acquired.[21] In addition to that, the difference in films can be avoided since the in situ measurement is carried out in the same film at the same specific point, through which more comparative data can be gained. In situ Raman investigation of lithium insertion into $V_2O_5$ thin films was performed by R. Baddour-Hadjean and his co-workers to describe the local structure changes during redox reactions.[22]

$^z$E-mail: zhanghl@nimte.ac.cn

In our previous work, as an alternative to ex situ Raman, an unconventional self-manufactured electrochemical in situ Raman technique was used to investigate structure variation of the nano-crystal-in-glass and layered $V_2O_5$ thin films in $Li^+$-based electrolyte. [23]

Here, we develop this powerful and sensitive in situ spectroscopic Raman measurement system as presented in Fig. 1a to monitor the local structure changes on the electrode-electrolyte interface of a layered $V_2O_5$ and $Zn^{2+}$-based electrolyte during the redox reaction. Tuning structural dynamics and charge transfer of $Zn^{2+}$ intercalation/deintercalation in the layered $V_2O_5$ electrodes by in situ Raman spectroelectrochemistry enables improved electrochemically stable performance due to the greater Coulombic force of $Zn^{2+}$ on $V_2O_5$ matrix than that of $Li^+$ for electrochromic devices.

## Experimental

***Preparation of the $V_2O_5$ thin film.***—To form the $V_2O_5$ precursor, 0.6 g of pure $V_2O_5$ powder was added into 8 ml of deionized water and stirred by a magnetic stirrer for 5 min. During the process of stirring, 3 ml of $H_2O_2$ solution (30 wt%) was added drop by drop, which slowly turned the solution from shallow yellow to bricklike red. Continue to stir for another 15 min to fully mix and 40 ml of deionized water was added. After that, an ultrasonic cell disruptor was used for 20 min to make the $V_2O_5$ particles uniformly disturbed in the solution. After a period of 7d aging in a sealed container, the solution can be used as a precursor following dilution by ethanol. Afterward, the $V_2O_5$ thin film was deposited in a two-electrode system using indium tin oxide (ITO) as the working electrode and Pt sheet as the counter electrode and ethanol solution of the precursor (10 vol%) as the electrolyte. The electrochemical deposition process was carried out in a thermostatic bath at 40 °C with a constant voltage at 8 V for 8 min. The obtained film was dried at 60 °C for 12 h in the air in the final process.

***Measurements.***—The structure of $V_2O_5$ thin film was analyzed through X-ray diffraction (XRD, Bruker D8 Advance using Cu-K$\alpha$ ($\lambda = 0.154178$ nm) radiation and a theta-2theta configuration and high resolution transmission electron microscopy (HRTEM, JEOL2100). In situ Raman measurements were carried out in a Renishaw inVia Reflex confocal Raman microscope (532 nm laser source), with 1% laser power, 5 s of exposure time, and 4 times of accumulation, in coordination with an electrochemical workstation (CHI660D, Chenhua, Shanghai). A self-designed electrochemical cell (Fig. 1a) was specifically optimized for Raman spectroscopy measurements, which used the obtained sample as the working electrode, a Pt wire as the counter electrode, a KCl-saturated Ag/AgCl as the reference electrode, and 0.4 M $Zn(CF_3SO_3)_2$ in propylene carbonate (PC) as electrolyte. In situ optical spectroscopy measurements were operated through a UV–vis-IR spectroscopy (Perkin-Elmer Lambda 950) in cooperation with the electrochemical workstation. In addition to that, cyclic voltammetry (CV) was performed in the electrochemical workstation (CHI660D, Chenhua, Shanghai).
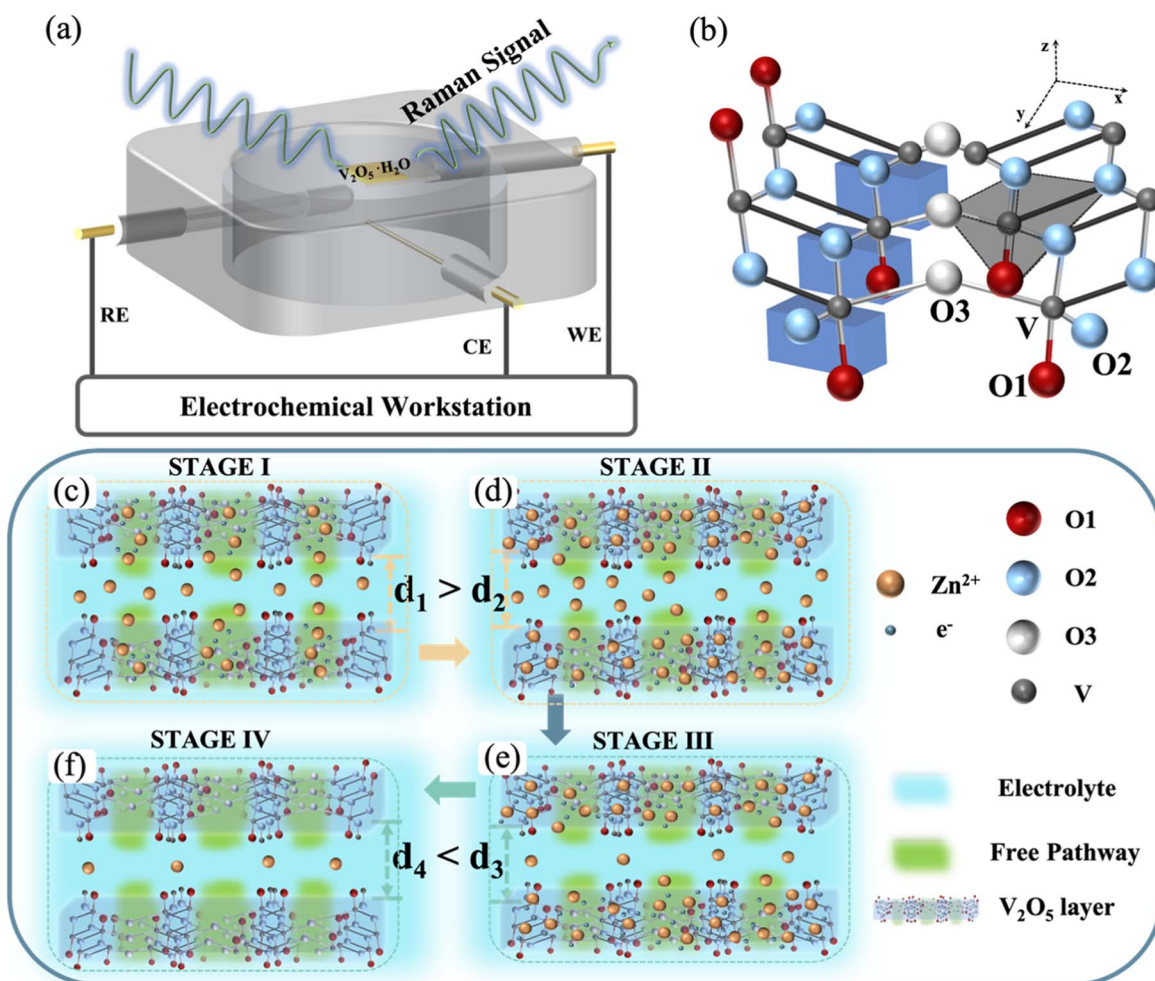


**Figure 1.** (a) Schematic diagram of the in situ Raman Characterization under a three-electrode mode. (b) Ball and stick model of classic $V_2O_5$ crystal. In the negative scan: (c) at the voltage from +1.8 V to +0.7 V conducting Zn ions insert into the interlayer and free pathway of $V_2O_5$ skeleton; (d) at the voltage from +0.7 V to +0.3 V conducting Zn ions insert into the whole $V_2O_5$ skeleton; In the positive scan: (e) at the voltage form −0.5 V to +0.5 V conducting Zn ions extract from the interlayer; (f) at the voltage from +0.5 V to +0.9 V conducting Zn ions extract from the whole space of $V_2O_5$ skeleton.
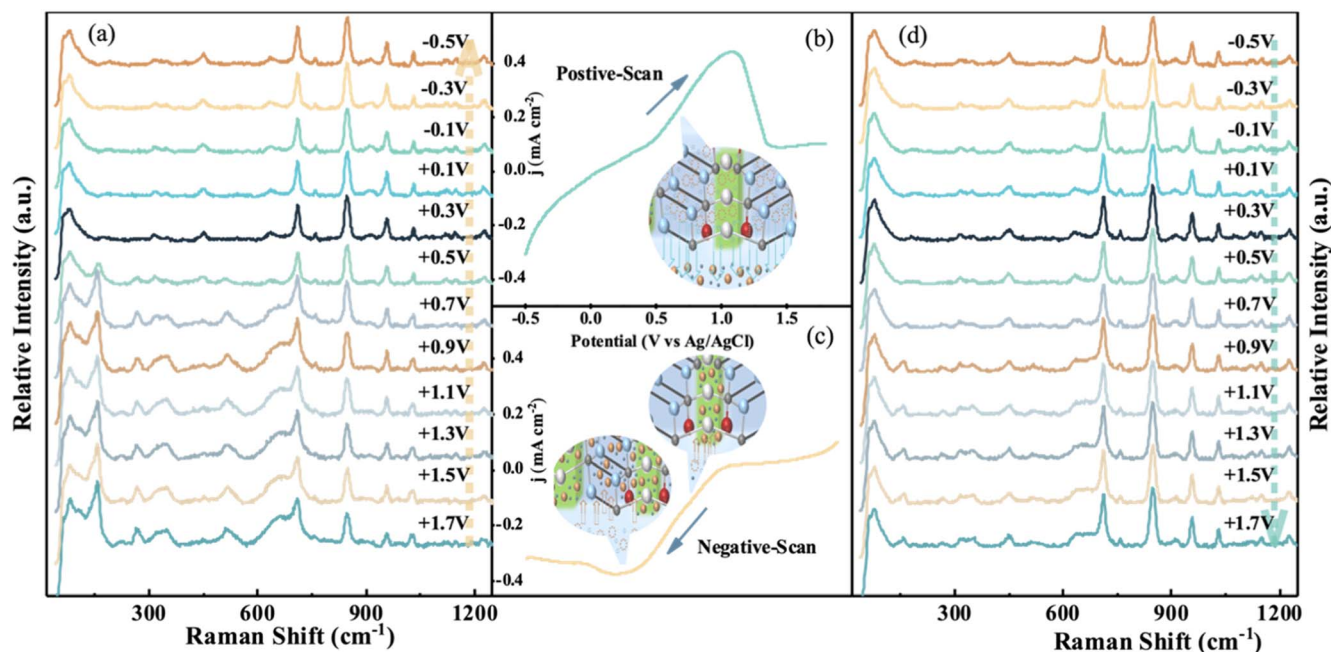
**Figure 2.** (a) Raman curve in the negative scan from +1.8 V to −0.5 V at the interval of 0.2 V. (b) CV curve for the negative scan. (c) CV curve for the positive scan. (d) Raman curve in the positive scan from −0.5 V to +1.8 V at the interval of 0.2 V.

## Results and Discussion

All detectable peaks from XRD patterns of the as-deposited $V_2O_5 \cdot H_2O$ thin film are indexed as $V_2O_5 \cdot H_2O$ (PDF #40-1296) as shown in Fig. S1a. A large interlayer distance of 1.28 nm is indicated by the strong (001) diffraction peak which facilitates the intercalation and the charge transfer of conducting Zn ions, and the multilayered structure can be clearly seen from the SEM cross-section image (Fig. S1b). In addition to that, amorphous structure can be determined by low intensity of (003) and (004), which corresponds to a relatively wide full width at half maximum (FWHM) of 3.32° and 2.31°, respectively. Considering the poor crystallinity of the as-deposited $V_2O_5 \cdot H_2O$ thin film and the limited accuracy of the XRD technique, the phase structure is further investigated by TEM and SEAD. It can be noted that no distinct crystalline phase exists, confirmed by diffused halo rings, as shown in Fig. S1d. Interestingly, the characteristics of nanocrystalline $V_2O_5$ can be confirmed in Fig. S1c. The data reported here appear to support the assumption that a layered $V_2O_5 \cdot H_2O$ thin film with the amorphous/crystalline coexisting phase is achieved. The n of crystal water in the layered $V_2O_5 \cdot nH_2O$ is calculated to be around 1 from the TGA result in Fig. S2. The typical crystal structure of $V_2O_5$ is presented in Fig. 1b. The vanadium atom (gray ball) is located within the oxygen pyramid (shaded area) in the classic crystal structure of $V_2O_5$. As indicated by the plot, there are three none-quivalent oxygen in the pyramid, noted by the different colors: red for $O_1$, blue for $O_2$, and white for $O_3$, respectively. Therefore, four different types of V–O bonds with different lengths can be observed from the ball-and-stick model. The strong and short apical bonds of V–$O_1$ have a length of 1.577 Å, and the bridge V–$O_3$ bonds with a length of 1.779 Å. And two different types of V–$O_2$, one as the "ladder step" (blue stairs) V–$O_2$ within the V–O chain has a distance of 1.878 Å and the other as the interchain V–$O_2$ (black stick) with a distance of 2.017 Å.

To monitor the chemical bonding evolution of $V_2O_5$ film during CV, the CV measurement was carried out at the scan rate of 4 mV s$^{-1}$ within the potential range of +1.8 V to −0.5 V, and in the meantime, Raman laser was shined on the surface of the $V_2O_5$ film to record the Raman signal at the different potential at an interval of 0.1 V. The complete CV curve is presented in Fig. S3. Multiple redox peaks can be distinguished from the curve, which reveals the

different steps of the insertion and extraction of $Zn^{2+}$ and electron into the $V_2O_5$ film as indicated by the equation: $xZn^{2+} + 2xe^- + V_2O_5 \cdot H_2O \leftrightarrow Zn_xV_2O_5 \cdot H_2O$. The split CV curves and the corresponding Raman spectrum are shown in Fig. 2 and the comparative Raman spectra of the electrolyte, as-deposited film are presented in Fig. S4a. As revealed in Fig. 2a, the general shape of the Raman spectrum is flat and the peaks are relatively broad, indicating the amorphous structure of our film, in accordance with the XRD result as shown in Fig. S1a.[24,25] As presented in Table I, the peak at 1027 cm$^{-1}$ and 976 cm$^{-1}$ is related to the stretching mode of V = $O_1$(apical bonds[26]) and V–$O_1$,[18] respectively. The peak at 650 cm$^{-1}$ and 526 cm$^{-1}$ is assigned to the stretching of V–$O_2$ (ladder step) and V–$O_2$ (interchain bonds) bonds, respectively.[18,24] The wide peak from 300–380 cm$^{-1}$ is quite complicated. Actually, the peaks in the frequency from 400 cm$^{-1}$ to 200 cm$^{-1}$ has considerable coupling effect. This wide peak from 300–380 cm$^{-1}$ is devoted to the bending vibration of V–$O_3$,[26,27,29] the bending vibration of $O_1$–V–$O_2$ and $O_1$–V–$O_3$.[18] These bonds are related to the largest vacancy in the $V_2O_5$ skeleton as indicated by Fig. 1a. That part in $V_2O_5$ skeleton has a low resistance for ions in the process of insertion and extraction, where the bending modes of V–$O_3$, $O_1$–V–$O_2$, and $O_1$–V–$O_3$ at 300–380 cm$^{-1}$ change first and then the other modes. Therefore, the combination of these bonds can be considered as the "free pathway" within the layers. The peak at 283 cm$^{-1}$ is related to the bending vibration of the V=O bonds.[29] Raman peak at low-frequency region can be assigned to in-phase rotation which can be seen as a pointer of the long-range ordering of the V–O framework in the plane.[26] In addition to that, low-frequency peaks are related to the lattice vibration, so the peaks at low frequency are strongly related to the layered structure.[25,28] The peak at 157 cm$^{-1}$ can be assigned to the displacement of the V atom along the y-axis,[30] the displacement in the xz plane disappeared due to our amorphous structure. In addition, the peak's intensity is extremely low compared to crystalized $V_2O_5$ in other works.[24,26]

In the negative scan (yellow arrow in Fig. 2c) with the insertion of Zn ion, an overall decrease of Raman peak (Fig. 2a) intensity is observed. The peak at 1027 cm$^{-1}$ is quite wide at the voltage of +1.7 V, but it becomes sharper as the negative scan goes on, which is related to the puckering of $V_2O_5 \cdot H_2O$ during insertion.[31] The enlarged plot of peak 1027 cm$^{-1}$ is demonstrated in Fig. S5.
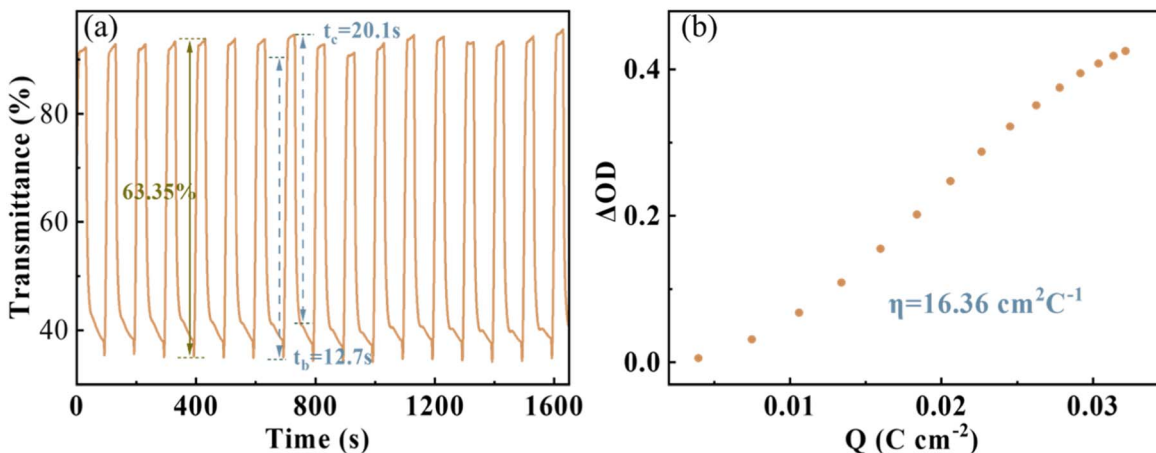
**Figure 3.** (a) Switching time and in situ transmittance spectrum at $\lambda = 800$ nm ($-0.5$ V$/ + 1.8$ V, 100 s per cycle). (b) Variation of the optical density ($\Delta OD$) and charge density (Q) at $\lambda = 800$ nm.

**Table I.** The contributions of Raman peaks for $V_2O_5$.

| Band peak (cm$^{-1}$) | Contributions | References |
|---|---|---|
| 1027 | Stretching of V=O$_1$ | 25 |
| 976 | Stretching of V–O$_1$ | 18 |
| 650 | Stretching of V–O$_2$ (ladder step) | 18 |
| 526 | Stretching of V–O$_2$ (interchain bonds) | 23 |
| 300–380 | Bending of V–O$_3$, O$_1$–V–O$_2$ and O$_1$–V–O$_3$ | 25–27 |
| 283 | Bending of V=O | 27 |
| 157 | Displacement of V atom along $y$-axis | 28 |

Throughout a full circle, the shape of this peak becomes sharper, which may be due to the squeeze of the inserted ion and electrons causing the rotation of the V atom and thus affecting its ordering.[32] Comparing with our previous work[23] on in situ Raman spectrum of Li$^+$-induced $V_2O_5 \cdot H_2O$, the peaks at 1027 cm$^{-1}$ and 976 cm$^{-1}$ change in a very slight extent (see Fig. S5 in supporting information), which is most likely due to the greater Coulombic force between Zn$^{2+}$ and the $V_2O_5$ skeleton. A smaller potential window ($-0.5$ V $\sim +1.7$ V) in Zn$^{2+}$-$V_2O_5$ system can gain coloration efficiency close to that ($-1.0$ V $\sim +2.0$ V) in Li$^+$- $V_2O_5$ system, which can be attributed to Zn$^{2+}$ enable $V_2O_5 \cdot H_2O$ with more efficient charge transfer than Li$^+$. Such a more subtle structural transformation and a smaller potential window can contribute theoretically to the long-term stability in Zn$^{2+}$-based electrochromic devices.

For the peaks in the range lower than 600 cm$^{-1}$, a general intensity decrease is observed in the negative scan, which indicates that the film becomes more disordered with the insertion of Zn ions.[18] The peaks at 157 cm$^{-1}$, 283 cm$^{-1}$, 300–380 cm$^{-1}$, 526 cm$^{-1}$, 560 cm$^{-1}$ barely change at the voltage from $+1.7$ V to $+0.9$ V. This indicates that the insertion of Zn$^{2+}$ at first mainly happens in the interlayer,[33,34] and due to the large interlayer distance of our film,[35] the intercalation of zinc in the interlayer area has a neglectable effect on the Raman peaks. When the potential gradually decreases from $+0.9$ V to $+0.7$ V, the intensity of the board peak at ranges from 300–380 cm$^{-1}$ related to the bending of O$_3$–V–O$_3$, O$_1$–V–O$_2$, and O$_1$–V–O$_3$ decreases (Fig. S4b). This implies the insertion of Zn and electron into the "free pathway" of $V_2O_5 \cdot H_2O$ within the layers. Therefore, the first-step insertion into layers happens at the "free pathway" of the $V_2O_5$ skeleton as revealed in the right callout plot of Fig. 2c. Reasonably, as the scan of voltage goes on, this peak gradually goes down due to the insertion happening in the whole other space of $V_2O_5$ skeleton. When the voltage arrives at $+0.3$ V, these peaks at 157 cm$^{-1}$, 283 cm$^{-1}$, 526 cm$^{-1}$, 300–380 cm$^{-1}$, and

650 cm$^{-1}$ become flat. The flatness of the peaks is caused by the insertion of the Zn ion into the whole $V_2O_5$ skeleton, which limits the bending vibration of the bonds. The detailed Raman curve changed by the interval of 0.1 V from $+0.9$ V to $+0.3$ V is given in Fig. S4b. Coordinating with the CV curve, $+0.7$ V is at the foot of the reduced peak, which indicates these Raman peaks are related to the second-step insertion of the Zn$^{2+}$ into the $V_2O_5$ skeleton as indicated by the left callout plot in Fig. 2c. At the potential range from $+0.3$ V to $-0.5$ V, no distinct Raman peaks variation can be discerned, which indicates that the insertion of Zn$^{2+}$ from interlayer space into the $V_2O_5$ skeleton was complete and the conducting Zn ions can no longer be inserted into the layer anymore. However, there is a quite flat peak in the CV around $-0.2$ V corresponding to the further insertion of Zn ions into the interlayer since part of the ion and electron has been transferred to the skeleton.

Noticeably, a reversed process can be seen in the positive scan as presented in Figs. 2c and 2d. When the opposite voltage is applied, the extraction of the ions starts. According to the CV curve, there is a wide peak in the range from $-0.5$ V to $+0.5$ V. Comparing the Raman spectrum at that potential range, the peaks remain flat, indicating the first-step extraction was the extraction of the ion from the interlayer. Only after an amount of ion was extracted from the interlayer, the extraction of ion from the $V_2O_5$ skeleton will start (as shown in the callout plot in Fig. 2c), which can be seen in the Raman spectrum from $+0.5$ V to $+0.9$ V (detailed change is plotted in Fig. S4c). Interestingly, as the same as the insertion process, this range of voltage is also the climbing part of the highest peak in CV. During this potential range, with the extraction of ions and electrons from the skeleton, the bonds start to resurrect. Noticeably, the peak around 300–380 cm$^{-1}$ synchronically recovered with other peaks under 600 cm$^{-1}$, meaning at this potential range zinc and electron in the $V_2O_5$ skeleton are extracted at the same time. Different from the insertion process, the exaction process is simpler and much easier than the process of insertion since the insertion encounters a lot of
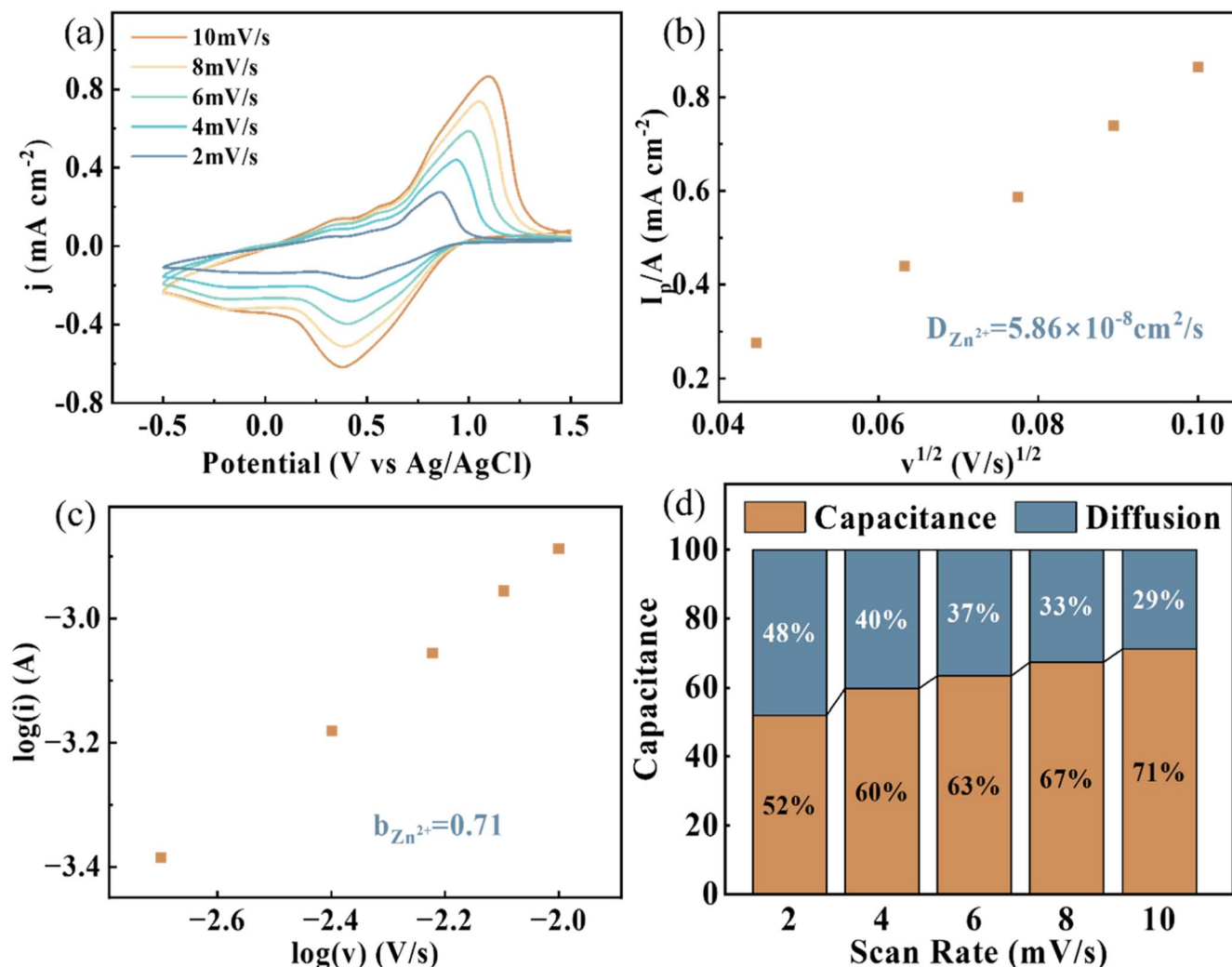
**Figure 4.** (a) CV curves of the $V_2O_5 \cdot H_2O$ thin film in 0.4 M $PC-Zn(CF_3SO_3)_2$ solution at the scan rates of 2, 4, 6, 8 and 10 mV s$^{-1}$, respectively. (b) The relationship between the peak current densities ($I_p$) and the square root of scan rate ($v^{1/2}$) and (c) power law dependence of the peak current vs the scan rate for the the$V_2O_5$ thin film in 0.4 M $PC-Zn(CF_3SO_3)_2$ solution. (d) The contribution of diffusion-controlled behavior at different scan rates of the $V_2O_5$ thin film.

obstacles like the electrostatic force between the ions and the $V_2O_5$ framework. Afterward, the peaks stabilized, which implies the completion of the extraction. However, all these peaks do not return to the original intensity when the voltage returns to $+1.7$ V, indicating that part of the inserted ions cannot be extracted, especially those inserted into the skeleton, which can also be confirmed by the inequivalent half in Galvanostatic charge/discharge curve as shown in Fig. S6.

To summarize, the insertion of zinc and electron into $V_2O_5 \cdot 1H_2O$ thin film causes the decrease of the interlayer distance, and the extraction recovers the spacing as revealed by our previous study and other's work.[35,36] The journey of zinc and electron is uncovered through in situ Raman spectroelectrochemistry. The insertion of $Zn^{2+}$ and electrons into the $V_2O_5 \cdot 1H_2O$ film can be divided into two stages. The first stage was the insertion into the interlayer space of the $V_2O_5 \cdot 1H_2O$ film. The second starts first in the "free pathway" of the $V_2O_5$ skeleton as shown in (Fig. 1c) and then in the other parts of the $V_2O_5$ skeleton (Fig. 1d). However, the extraction was quite simpler, first extracted from the interlayer space as indicated by Fig. 1e, and then from the $V_2O_5$ skeleton as shown in Fig. 1f. This journey of $Zn^{2+}$ and electrons within the film was believed to be the cause of the difference in switching time, in which the coloration time is longer than the bleaching time.

In situ time-dependent transmittance spectra at $\lambda = 800$ nm are executed to find out the electrochromic parameters of the $V_2O_5 \cdot H_2O$

film in the $Zn^{2+}$-based electrolyte. The applied voltage is 1.8 V for the 40 s and $-0.5$ V for 40 s. As revealed in Fig. 3a, the highest transmittance is up to 95.62% in the bleached state and the maximum transmittance modulation ($\Delta T$) is estimated to be 63%, which is much higher than that of $Li^+$: 30% at 780 nm for $V_2O_5$ film on FTO[37] and 68.94% at 800 nm for $V_2O_5$ on graphene.[38] The high transmittance modulation is mainly caused by the inert advantage of the $Zn^{2+}$ with a comparative radius but twice the valence of $Li^+$. In addition to that, the lubricating effect[39] of structural $H_2O$ in $V_2O_5$ reduced the electrostatic interactions between Zn ions and the $V_2O_5$ skeleton, which in turn deepened the insertion of ions and electrons. Also, the nanocrystal in layered structure has a buffering effect[40] on the insertion which elongates the insertion process. The colored and bleached switching time can be defined as the time required for the change of transmittance of the film to reach 90% of the maximum. The coloration time is estimated to be 20.1 s and the bleaching 12.7 s. The coloration time of the $V_2O_5 \cdot H_2O$ film is longer, whereas the bleaching time is shorter. The longer coloration time is due to the relatively strong electrostatic interaction between the $Zn^{2+}$ and the $V_2O_5$ skeleton, and the difficulty for the conducting Zn ions to enter the $V_2O_5$ skeleton. However, the extraction is comparatively easier, which results in a shorter time for bleaching. This result is in perfect concordance with the result we drew from in situ Raman analysis. Coloration efficiency ($\eta$), the optical density change ($\Delta OD$) in response to the stored charge per unit area (q), is another important

criterion for electrochromic materials. This factor can be calculated by the equation: $\eta = \Delta OD/q = \log(T_{bleached}/T_{colored})/q$, where $\Delta OD$ is the change of optical density, q is the inserted (extracted) charge per unit area, $T_{bleached}$ is the transmittance in bleached state, and $T_{colored}$ is the transmittance in colored state. The $\eta$ is estimated to be $16.36\ cm^2\ C^{-1}$ in our case.

The electrochemical properties of $V_2O_5 \cdot H_2O$ are further investigated by CV under the potential range from $-0.5$ V to $1.5$ V vs Ag/AgCl at different scan rates. As shown in Fig. 4a, all the curves exhibit similar shapes, confirming good reversibility, and multiple redox peaks further confirmed the multi-step of the ions insertion and extraction. As the scan rate increased from $2\ mV\ s^{-1}$ to $10\ mV\ s^{-1}$ the gap between redox peaks increased, which indicated the increase of internal diffusion resistance due to the polarization effect of the electrode.[41] And thus limited the insertion (extraction) of zinc and electrons into $V_2O_5 \cdot H_2O$ film. The response time of an electrochromic device, one of the important factors, is strongly deepened on the ion diffusion coefficient and ion diffusion distance. The diffusion coefficient (D) can be calculated by the Randles-Sevcik law, using the following equation: $i_p = 2.69 \times 10^5 A C_0 D^{1/2} n^{3/2} v^{1/2}$, in which: $i_p$ (A) represents the peak current, $A$ (cm$^2$) the electrode area, $C_0$ (mol·cm$^{-3}$) the concentration of the electrolyte, $n$ the number of the electrons transferred in the reaction, and $v$ (mV·s$^{-1}$) the scan rate. Perfect linear correlation of $i_p$ and $v^{1/2}$, indicated by the Person correlation coefficient of 0.99, reveals that the electrode process is diffusion controlled. The D of $Zn^{2+}$ was calculated to be $5.86 \times 10^{-8}$. Both large interlayer distance and inherent advantage of $Zn^{2+}$ (small radius and large electrostatic force) contribute to the large diffusion coefficient. The "b" value can be obtained from the relationship $i = av^b$, where $i$ (A) is the peak current and $v$ is the scan rate. The logarithmic curve of this equation was plotted in Fig. 4c. After liner fitting, "b" is calculated to be around 0.71 within the range of 0.5 to 1, which indicated that pseudocapacitive charge storage was the main contribution for capacity contribution. As shown in Fig. 4d, the percentage of capacitive charge in the whole charge rose from 52 to 71 with the increase of the scan rate. The scan rate affects the contribution of capacitive charge and diffusion-controlled charge. When the scan rate is low, diffusion-controlled charge is present since there was enough time for the conducting Zn ions to diffuse into the inner structure; however, the contribution of capacitive charge becomes more dominant at a higher scan rate. And this result has a great concordance with the aforenoted "b" value.

## Conclusions

We have shown some of the possibilities of using in situ Raman spectroelectrochemistry to illumine the chemical bonding evolution of $V_2O_5 \cdot H_2O$ and the charge transfer of a layered $V_2O_5 \cdot H_2O$ in a $Zn^{2+}$-based electrolyte. The use of spectroelectrochemical experiments allows researchers to reach a better control of the potential through the three-electrode setup. One of the most important consequences of the higher applied potentials is the observation of a $Zn^{2+}$-based electrochemical doping effect in the layered $V_2O_5 \cdot H_2O$ causing an obvious increase in intensity of the V-O band at positive potentials. In particular, the existence of free channels, such as "free pathway" and large interlayer space, in the internal environment of the layered $V_2O_5 \cdot 1H_2O$ is potentially advantageous as these can be highly reversible to the electrochemical and electrochromic systems. Furthermore, the employment of the small radius $Zn^{2+}$ and the layered $V_2O_5 \cdot H_2O$ can achieve an extremely high transmittance of 95.62% at 800 nm, a high transmittance modulation of 63%, and a quick bleached time of 12.7 s. A comparative analysis of structural transformation and potential window of the layered $V_2O_5 \cdot H_2O$ electrodes in between $Zn^{2+}$-based and $Li^+$-based electrolytes indicates that $Zn^{2+}$-$V_2O_5 \cdot H_2O$ system enjoys the merit of multivalent $Zn^{2+}$. These results will provide a better theoretical and experimental basis for understanding the behaviors and efficiency of electrochromic and energy storage electrode materials in multivalent electrolyte systems.

## ORCID

Hongtao Cao https://orcid.org/0000-0002-4458-4621
Hongliang Zhang https://orcid.org/0000-0002-9295-8683

## References

1. C. G. Granqvist, M. A. Arvizu, İ. B. Pehlivan, H.-Y. Qu, R.-T. Wen, and G. A. Niklasson, "Electrochromic materials and devices for energy efficiency and human comfort in buildings: A critical review." *Electrochim. Acta*, **259**, 1170 (2018).
2. T. Niwa and O. Takai, "All-solid-state reflectance-type electrochromic devices using iridium tin oxide film as counter electrode." *Thin Solid Films*, **518**, 5340 (2010).
3. J. Tu, G. Zhao, W. Wang, X. Wang, X. H. Xia, and C. Gu, "A multicolor electrochromic film based on a SnO$_2$/V$_2$O$_5$ core/shell structure for adaptive camouflage." *J. Mater. Chem. C*, **7**, 5702 (2019).
4. C. Qi, C. Chen, T. Huang, Z. Zhang, Z. Huang, Y. Zhan, X. Tang, and J. Y. Luo, "Greatly simplified all-solid-state camera shielding device of mobile phone based on the shoulder-by-shoulder electrochromic technology." *ACS Applied Electronic Materials*, **3**, 2631 (2021).
5. C. Gu, A.-B. Jia, Y.-M. Zhang, and S. X.-A. Zhang, "Emerging electrochromic materials and devices for future displays." *Chem. Rev.*, **122**, 14679 (2022).
6. S. Deb, "A novel electrophotographic system." *Appl. Opt.*, **8**, 192 (1969).
7. N. Zhang, Y. Dong, M. Jia, X. Bian, Y. Wang, M. Qiu, J. Xu, Y. Liu, L. Jiao, and F. Cheng, "Rechargeable aqueous Zn–V$_2$O$_5$ battery with high energy density and long cycle life." *ACS Energy Lett.*, **3**, 1366 (2018).
8. H. Li, C. J. Firby, and A. Y. Elezzabi, "Rechargeable aqueous hybrid Zn$^{2+}$/Al$^{3+}$ electrochromic batteries." *Joule*, **3**, 2268 (2019).
9. D. Wei, M. R. Scherer, C. Bower, P. Andrew, T. Ryhänen, and U. Steiner, "A nanostructured electrochromic supercapacitor." *Nano Lett.*, **12**, 1857 (2012).
10. I. Mjejri, M. Gaudon, and A. Rougier, "Mo addition for improved electrochromic properties of V$_2$O$_5$ thick films." *Sol. Energy Mater. Sol. Cells*, **198**, 19 (2019).
11. Y.-S. Hsiao, C.-W. Chang-Jian, W.-L. Syu, S.-C. Yen, J.-H. Huang, H.-C. Weng, C.-Z. Lu, and S.-C. Hsu, "Enhanced electrochromic performance of carbon-coated V$_2$O$_5$ derived from a metal–organic framework." *Appl. Surf. Sci.*, **542**, 148498 (2021).
12. J. Song, L. Wang, Y. Lu, J. Liu, B. Guo, P. Xiao, J.-J. Lee, X.-Q. Yang, G. Henkelman, and J. B. Goodenough, "Removal of interstitial H$_2$O in hexacyanometallates for a superior cathode of a sodium-ion battery." *J. Am. Chem. Soc.*, **137**, 2658 (2015).
13. A. Mukherjee, N. Sa, P. J. Phillips, A. Burrell, J. Vaughey, and R. F. Klie, "Direct investigation of Mg intercalation into the orthorhombic V$_2$O$_5$ cathode using atomic-resolution transmission electron microscopy." *Chem. Mater.*, **29**, 2218 (2017).
14. Z. Wang, Z. Ruan, Z. Liu, Y. Wang, Z. Tang, H. Li, M. Zhu, T. F. Hung, J. Liu, and Z. Shi, "A flexible rechargeable zinc-ion wire-shaped battery with shape memory function." *J. Mater. Chem. A*, **6**, 8549 (2018).
15. H. Eric and H. Li, "Rechargeable Zn$^{2+}$/Al$^{3+}$ dual-ion electrochromic device with long life time utilizing dimethyl sulfoxide (DMSO)-nanocluster modified hydrogel electrolytes." *RSC Adv.*, **9**, 32047 (2019).
16. H. Li, L. McRae, C. J. Firby, and A. Y. Elezzabi, "Rechargeable aqueous electrochromic batteries utilizing Ti-substituted tungsten molybdenum oxide based Zn$^{2+}$ ion intercalation cathodes." *Adv. Mater.*, **31**, 1807065 (2019).
17. J. Zhang, R. Wang, X. Yang, W. Lu, X. Wu, X. Wang, H. Li, and L. Chen, "Direct observation of inhomogeneous solid electrolyte interphase on MnO anode with atomic force microscopy and spectroscopy." *Nano Lett.*, **12**, 2153 (2012).
18. R. Baddour-Hadjean, J. Pereira-Ramos, C. Navone, and M. Smirnov, "Raman microspectrometry study of electrochemical lithium intercalation into sputtered crystalline V$_2$O$_5$ films." *Chem. Mater.*, **20**, 1916 (2008).
19. X. Liu, H. Euchner, M. Zarrabeitia, X. Gao, G. A. Elia, A. Groß, and S. Passerini, "Operando pH measurements decipher H$^+$/Zn$^{2+}$ intercalation chemistry in high-performance aqueous Zn/δ-V$_2$O$_5$ batteries." *ACS Energy Lett.*, **5**, 2979 (2020).
20. J.-X. Zheng, S.-Q. OuYang, L. Feng, J.-J. Sun, Z.-W. Xuan, and J.-H. Fang, "In-situ Raman spectroscopic studies on electrochemical oxidation behavior of chromium in alkaline solution." *J. Electroanal. Chem.*, **921**, 116682 (2022).
21. C. Korzeniewski, E. M. Peterson, J. P. Kitt, S. D. Minteer, and J. M. Harris, "Adapting confocal Raman microscopy for in situ studies of redox transformations at electrode-electrolyte interfaces." *J. Electroanal. Chem.*, **896**, 115207 (2021).
22. R. Baddour-Hadjean, C. Navone, and J. Pereira-Ramos, "In situ Raman microspectrometry investigation of electrochemical lithium intercalation into sputtered crystalline V$_2$O$_5$ thin films." *Electrochim. Acta*, **54**, 6674 (2009).
23. Z. Zhang, W. Xie, J. Li, H. Zhang, Q. Wang, C. Zhang, G. Xu, J. Gao, A. Rogachev, and H. Cao, "In situ raman observation of dynamically structural transformation induced by electrochemical lithium intercalation and deintercalation from multi-electrochromic V$_2$O$_5$ thin films." *Adv. Mater. Interfaces*, **9**, 26 2200883 (2022).

24. S.-H. Lee, H. M. Cheong, M. Je Seong, P. Liu, C. E. Tracy, A. Mascarenhas, J. R. Pitts, and S. K. Deb, "Microstructure study of amorphous vanadium oxide thin films using raman spectroscopy." *J. Appl. Phys.*, **92**, 1893 (2002).

25. S.-H. Lee, H. M. Cheong, M. J. Seong, P. Liu, C. E. Tracy, A. Mascarenhas, J. R. Pitts, and S. K. Deb, "Raman spectroscopic studies of amorphous vanadium oxide thin films." *Solid State Ionics*, **165**, 111 (2003).

26. A. Jarry, M. Walker, S. Theodoru, L. J. Brillson, and G. W. Rubloff, "Elucidating structural transformations in $Li_xV_2O_5$ electrochromic thin films by multimodal spectroscopies." *Chem. Mater.*, **32**, 7226 (2020).

27. A. Jin, W. Chen, Q. Zhu, Y. Yang, V. Volkov, and G. Zakharova, "Structural and electrochromic properties of molybdenum doped vanadium pentoxide thin films by sol–gel and hydrothermal synthesis." *Thin Solid Films*, **517**, 2023 (2009).

28. L. Abello, E. Husson, Y. Repelin, and G. Lucazeau, "Vibrational spectra and valence force field of crystalline $V_2O_5$." *Spectrochimica Acta Part A: Molecular Spectroscopy*, **39**, 641 (1983).

29. C. Julien, G. Nazri, and O. Bergström, "Raman scattering studies of microcrystalline $V_6O_{13}$." *Physica Status Solidi B Basic Research*, **201**, 319 (1997).

30. D. Huo, A. Contreras, B. Laïk, P. Bonnet, K. Guérin, D. Muller-Bouvet, C. Cenac-Morthe, R. Baddour-Hadjean, and J.-P. Pereira-Ramos, "Evidence for a nanosize effect on the structural and high performance electrochemical properties of $V_2O_5$ obtained via fluorine chemistry." *Electrochim. Acta*, **245**, 350 (2017).

31. R. Baddour-Hadjean, E. Raekelboom, and J. Pereira-Ramos, "New structural characterization of the $Li_xV_2O_5$ system provided by raman spectroscopy." *Chem. Mater.*, **18**, 3548 (2006).

32. G. Zhang, T. Xiong, X. Pan, Y. Zhao, M. Yan, H. Zhang, B. Wu, K. Zhao, and L. Mai, "Illumining phase transformation dynamics of vanadium oxide cathode by multimodal techniques under operando conditions." *Nano Res.*, **12**, 905 (2019).

33. X. Peng, X. Zhang, L. Wang, L. Hu, S. H. S. Cheng, C. Huang, B. Gao, F. Ma, K. Huo, and P. K. Chu, "Hydrogenated $V_2O_5$ nanosheets for superior lithium storage properties." *Adv. Funct. Mater.*, **26**, 784 (2016).

34. J. Braithwaite, C. Catlow, J. Gale, and J. Harding, " Lithium intercalation into vanadium pentoxide: a theoretical study." *Chem. Mater.*, **11**, 1990 (1999).

35. C. Wang, X. Zhang, S. Liu, H. Zhang, Q. Wang, C. Zhang, J. Gao, L. Liang, and H. Cao, "Interfacial charge transfer and zinc ion intercalation and deintercalation dynamics in flexible multicolor electrochromic energy storage devices." *ACS Appl. Energy Mater.*, **5**, 88 (2021).

36. F. Wu, Y. Wang, P. Ruan, X. Niu, D. Zheng, X. Xu, X. Gao, Y. Cai, W. Liu, and W. Shi, "Fe-doping enabled a stable vanadium oxide cathode with rapid Zn diffusion channel for aqueous zinc-ion batteries." *Materials Today Energy*, **21**, 100842 (2021).

37. W. He, Y. Liu, Z. Wan, and C. Jia, "Electrodeposition of $V_2O_5$ on $TiO_2$ nanorod arrays and their electrochromic properties." *RSC Adv.*, **6**, 68997 (2016).

38. J. Wu, D. Qiu, H. Zhang, H. Cao, W. Wang, Z. Liu, T. Tian, L. Liang, J. Gao, and F. Zhuge, "Flexible electrochromic $V_2O_5$ thin films with ultrahigh coloration efficiency on graphene electrodes." *J. Electrochem. Soc.*, **165**, D183 (2018).

39. M. Yan, P. He, Y. Chen, S. Wang, Q. Wei, K. Zhao, X. Xu, Q. An, Y. Shuang, and Y. Shao, "Water-lubricated intercalation in $V_2O_5 \cdot nH_2O$ for high-capacity and high-rate aqueous rechargeable zinc batteries." *Adv. Mater.*, **30**, 1703725 (2018).

40. A. Llordes, G. Garcia, J. Gazquez, and D. J. Milliron, "Tunable near-infrared and visible-light transmittance in nanocrystal-in-glass composites." *Nature*, **500**, 323 (2013).

41. P. Yang, P. Sun, L. Du, Z. Liang, X. Xie, X. Cai, L. Huang, S. Tan, and W. Mai, "Quantitative analysis of charge storage process of tungsten oxide that combines pseudocapacitive and electrochromic properties." *J. Phys. Chem. C*, **119**, 16483 (2015).